Seasonal variability of the South Equatorial Countercurrent

Shuiming Chen and Bo Qiu
Department of Oceanography, University of Hawaii at Manoa, Honolulu, Hawaii, USA

Received 11 December 2003; revised 7 May 2004; accepted 9 June 2004; published 5 August 2004.

[1] Using the 1.5-layer long Rossby wave model forced by the seasonal European Remote Sensing (ERS) satellite scatterometer wind, we demonstrate that the seasonal variability of the South Equatorial Countercurrent (SECC) is due to the interplay of two types of forced Rossby waves: the resonantly forced Rossby waves north of 10°S and the locally forced Rossby waves south of 10°S. The resonantly forced Rossby waves north of 10°S are due to the annually varying tropical Pacific wind, and the locally forced Rossby waves south of 10°S in the western basin are associated with the Western Pacific Monsoon. Both types of waves are intensified westward in the SECC region but have different phases across the SECC; this latitudinal phase jump results in the seasonal variability of the SECC, which reaches its maximum in March and its minimum in August. Favorable agreement between the seasonal SECC signals from the model and from the satellite sea surface height measurements confirms this new insight about the seasonal modulation of the SECC. *INDEX TERMS:* 4231 Oceanography: General: Equatorial oceanography; 4227 Oceanography: General: Diurnal, seasonal, and annual cycles; 4512 Oceanography: Physical: Currents; *KEYWORDS:* SECC, seasonal variability, Rossby waves

Citation: Chen, S., and B. Qiu (2004), Seasonal variability of the South Equatorial Countercurrent, *J. Geophys. Res.*, *109*, C08003, doi:10.1029/2003JC002243.

1. Introduction

[2] The South Equatorial Countercurrent (SECC) is located between 8°S and 11°S in the western South Pacific. Its eastward flow is mainly confined above the main thermocline (~200 m) with a mean speed of several cm s^{-1} (see Figures 1a and 1b). Embedded in the stronger and broader westward South Equatorial Current (SEC), the existence of the mean SECC can be understood as a wind-driven Sverdrup flow (see Figure 1c, in which we have assumed that the zonal Sverdrup transport resides in the upper 200 m). Meridionally, the negative mean wind stress curl in the SECC region [cf. *Kessler et al.*, 2003, Figure 5] generates a southward Sverdrup flow. As a result, the mean SECC turns south to join the SEC, as sketched by *Tomczak and Godfrey* [1994]. Near the Solomon Islands, the mean SECC is supplied by the return SEC on the northern side and by the North Queensland Current on the southern side, as suggested by *Qu and Lindstrom* [2002].

[3] The SECC has significant seasonal variability. As seen in the direct velocity measurements along 165°E during 1984–1991 [*Gouriou and Toole*, 1993], the SECC was about 20 cm s^{-1} eastward for the May–October period and about 5 cm s^{-1} eastward for the November–April period. Similar variability was seen in their dynamic calculation relative to 600 dbar. The mean velocity sections for both the May–October and November–April periods showed that the SECC was clearly above the 200 m depth. However, snapshot velocity sections showed that the SECC could reach as deep as ~250 m [*Delcroix et al.*, 1992]. On the basis of the optimal function fitting of the buoy drifts and current meter records between January 1987 and April 1992, *Reverdin et al.* [1994] showed that the SECC at 15 m along 162°E was about 20 cm s^{-1} eastward from January to March and about 5 cm s^{-1} westward from July to September. The surface zonal geostrophic flow from the WOA01 climatology (Figure 2) [*Conkright et al.*, 2002] also shows clear seasonality, although its magnitude is much smaller than the in situ measurements.

[4] With respect to the seasonal variability in the SECC, the previous studies by *Kessler* [1990] and *Wang et al.* [2000] emphasized that the phase of the annual harmonic of the thermocline depth anomaly changes abruptly across the zonal SECC. In other words, the thermocline depths on the southern and northern sides of the SECC fluctuate out of phase. Since the SECC exists above the main thermocline, its variability can be adequately described by a 1.5-layer reduced-gravity model in which the sea surface height (SSH) anomaly is proportional to the thermocline depth anomaly. The annual harmonic fitting of the decade-long Archiving, Validation, and Interpretation of Satellite Oceanographic Data (AVISO) altimetric SSH anomaly clearly demonstrates the phase jump across the SECC from 150–170°E within 1° latitude (Figure 3b). Notice that *Kessler* [1990] and *Wang et al.* [2000] used 2° latitude × 5° longitude and 1° latitude × 3° longitude gridded data sets, respectively, and that the AVISO altimetric SSH anomaly data set used for Figure 3 has a 1/3° × 1/3° resolution. According to geostrophy, a north-south phase jump in the thermocline depth or SSH can result in the modulation of a zonal jet. The effect will be maximized if the phase jump is 180° (i.e., out of phase) as

0148-0227/04/2003JC002243$09.00

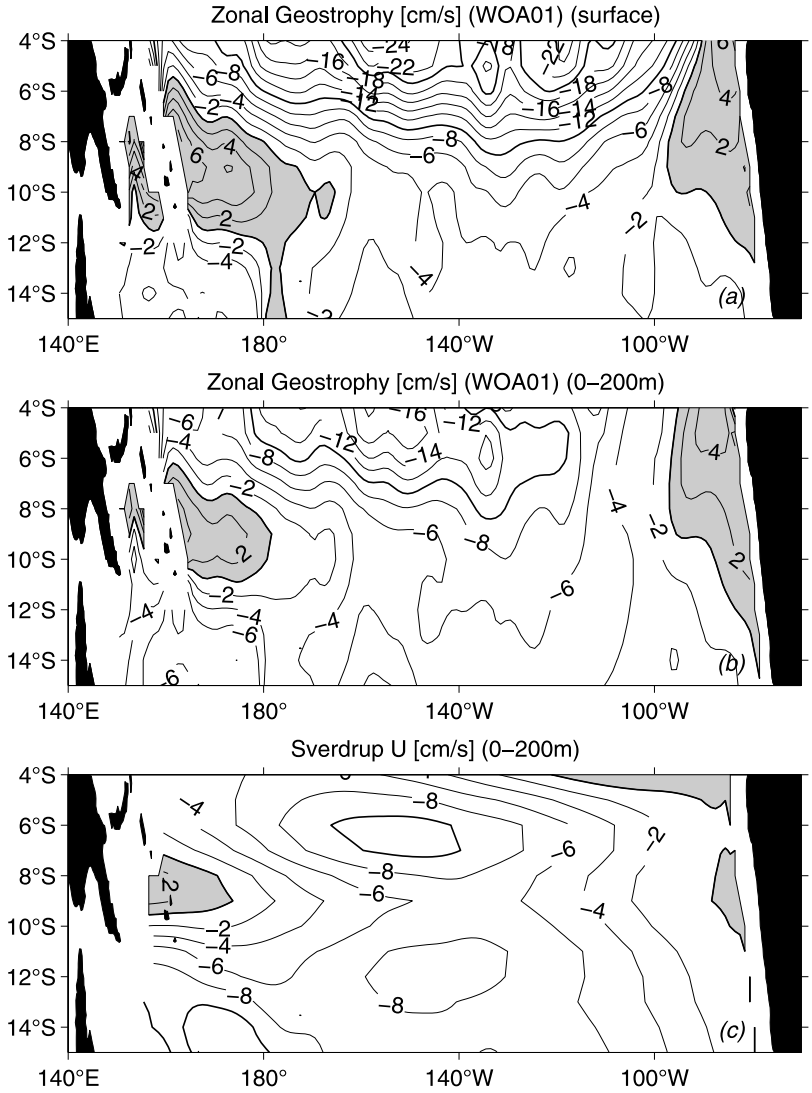

Figure 1. (a) Surface zonal geostrophy (0/1500 dbar) based on WOA01 [*Conkright et al.*, 2002]. (b) The 0–200 m average of the zonal geostrophy (0/1500 dbar) based on WOA01. (c) Sverdrup U from the 10-year mean of the ERS wind stress. The Sverdrup flow is assumed to reside in the upper 200 m. Positives are shaded. All contours are in cm s^{-1}.

suggested in Figure 3b. Therefore the phase jump in SSH anomaly or thermocline depth anomaly is a manifestation of the seasonal variation of the SECC.

[5] The main question to be addressed in this study is why the phase jump happens, or what causes the seasonal variability of the SECC? A similar phase jump was observed across the North Equatorial Countercurrent (NECC), the Northern Hemisphere counterpart of the SECC. *Kessler* [1990] suggested that the phase jump across the NECC was due to the seasonal migration of the Intertropical Convergence Zone (ITCZ). *Wang et al.* [2000] argued that the phase jump across the SECC resulted from the merging of two different regimes: a local Ekman forcing dominant one (“Ekman regime”) and a Rossby wave adjustment dominant one (“Rossby wave regime”), based primarily on numerical experiments of a nonlinear model. The numerical model has one mixed layer and one active layer overlaying a deep inert layer. When forced only by the Western Pacific Monsoon wind stress (west to the dateline), the model can capture most of the annual variability of the thermocline depth south of the SECC but not north of the SECC. For the latter, the wind forcing east of the dateline in the South Pacific plays an important role through the Rossby wave propagation. Therefore they demonstrated that based on the numerical experiments, the Ekman and Rossby wave regimes prevail south and north of the SECC, respectively.

[6] Since the focus of *Wang et al.* [2000] was to examine the basinwide thermocline variability, regional dynamics relating to the SECC were not further explored. For example, north of the SECC, the time difference between the maximum seasonal thermocline depth and the minimum seasonal Ekman pumping is close to zero. This zero time difference suggests that the seasonal wind forcing and the ocean response propagate westward at similar speeds. *White* [2001] presented evidence for the annual coupled Rossby waves in the eastern South Pacific (20°S–5°S and 170°W to the eastern boundary). In this paper we present evidence for the resonantly forced Rossby waves north of the SECC in

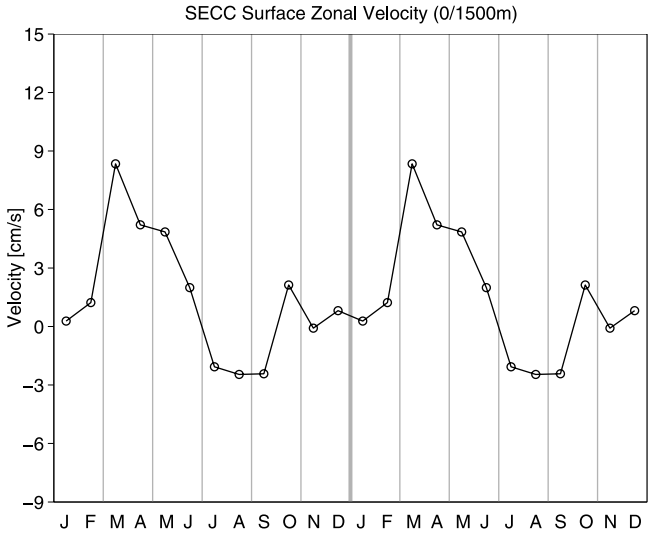

Figure 2. Zonal surface geostrophic velocity averaged over 13°S—8°S and 170°E—180°E. The velocity is calculated from the monthly mean temperature and salinity data sets of WOA01 [*Conkright et al.*, 2002].

the western South Pacific. South of the SECC, the westward propagation is seen in the seasonal thermocline depths while the local wind forcing is shown to be dominant [*Wang et al.*, 2000]. Therefore, south of the SECC, there is probably an interference of the forced Rossby waves and the free Rossby waves. The east-west extent of the wind forcing by the Western Pacific Monsoon is close to the annual Rossby wave length, which is about 43° longitude assuming that the Rossby waves propagate westward at a speed about 0.15 m s^{-1}. Because of this particular setting, we are able to identify the doubling of the Rossby wave westward propagation speed as illustrated by *Qiu et al.* [1997]. Here "doubling" means that the propagation speed derived from the altimetric SSH anomaly data doubles the propagation speed used in the 1.5-layer Rossby wave model.

[7] In this study, we will test the hypothesis that the seasonal variability of the SECC is due to the interplay of two types of forced Rossby waves: the resonantly forced ones and the locally forced ones. To illustrate the dynamics of the resonantly and locally forced Rossby waves, we adopt the 1.5-layer model with the decade-long European Remote Sensing (ERS) satellite microwave scatterometers wind data [*WOCE Data Products Committee*, 2002] and altimetric SSH anomaly data sets. The 1.5-layer vorticity model with the longwave approximation has been applied to the tropical North Pacific [e.g., *Meyers*, 1979; *Kessler*, 1990] and to the eastern South Pacific [*Vega et al.*, 2003].

[8] In the next section, we will present the 1.5-layer model, its general solution, and two specific solutions under the wind fields relevant to this study. Numerical solutions of the Rossby waves forced by the seasonal ERS wind are presented in section 3. An examination of the wind follows in section 4. Section 5 provides the summary and discussion.

2. The 1.5-Layer Model

[9] Under the longwave approximation, the 1.5-layer linear quasi-geostrophic potential vorticity equation with wind forcing is [*White*, 1977; *Meyers*, 1979; *Qiu et al.*, 1997]

$$\frac{\partial h}{\partial t} - c_R \frac{\partial h}{\partial x} = -\frac{g'}{g} \nabla \times \frac{\vec{\tau}}{\rho_0 f}, \tag{1}$$

where h is the sea surface height,

$$c_R = \beta \frac{g' H_0}{f^2} = \beta \frac{c_1^2}{f^2}, \tag{2}$$

H_0 is the mean depth of the active upper layer, c_1 is the internal gravity wave speed, and the other notations are conventional. The right-hand side of equation (1) will be referred to as the wind forcing in this study, i.e.,

$$F(x, y; t) = -\frac{g'}{g} \nabla \times \frac{\vec{\tau}}{\rho_0 f}.$$

Notice that $F(x, y; t)$ is proportional to the Ekman pumping velocity w_E,

$$w_E = \nabla \times \frac{\vec{\tau}}{\rho_0 f}.$$

Since equation (1) is a one-dimensional (in x) first-order wave equation with westward characteristics, we can integrate the equation along any latitude from the eastern boundary without knowledge of other latitudes.

[10] *Kessler* [1990] discussed the assumptions used in the 1.5-layer model, such as the longwave approximation and neglect of mean flow. Despite those assumptions, the favorable comparison between the model results and the altimetric SSH observation in the SECC region in the next section suggests that equation (1) captures the relevant dynamics for the present study.

[11] When integrating equation (1), c_R is assumed to be unknown and then chosen through the best fitting between the model h field from equation (1) and the altimetric SSH anomaly field. The altimetric observation shows that the propagation of the long Rossby waves in most of the world oceans does not follow equation (2) but exceeds it [*Chelton and Schlax*, 1996]. Possible causes for this enhancement were summarized by *Fu and Chelton* [2001]. Treating c_R as an unknown was used before in the tropical Pacific by *Meyers* [1979] and by *Kessler* [1990].

[12] We will assume $h = 0$ at the eastern boundary (denoted as x_e), excluding Rossby waves emanating from the eastern boundary. Those Rossby waves are likely dissipated within tens of degrees longitude [*Fu and Qiu*, 2002; *Vega et al.*, 2003], resulting in insignificant influence on the SECC region in the western basin.

[13] The general solution and several specific solutions of equation (1) for various wind forcings are given by *White* [1977] and *Meyers* [1979]. The following summary of analytical solutions, related to the present study, serves to define some terminology and will be used to interpret observations and model outputs. The spatial amplitude and phase patterns of h, relative to F, are emphasized here.

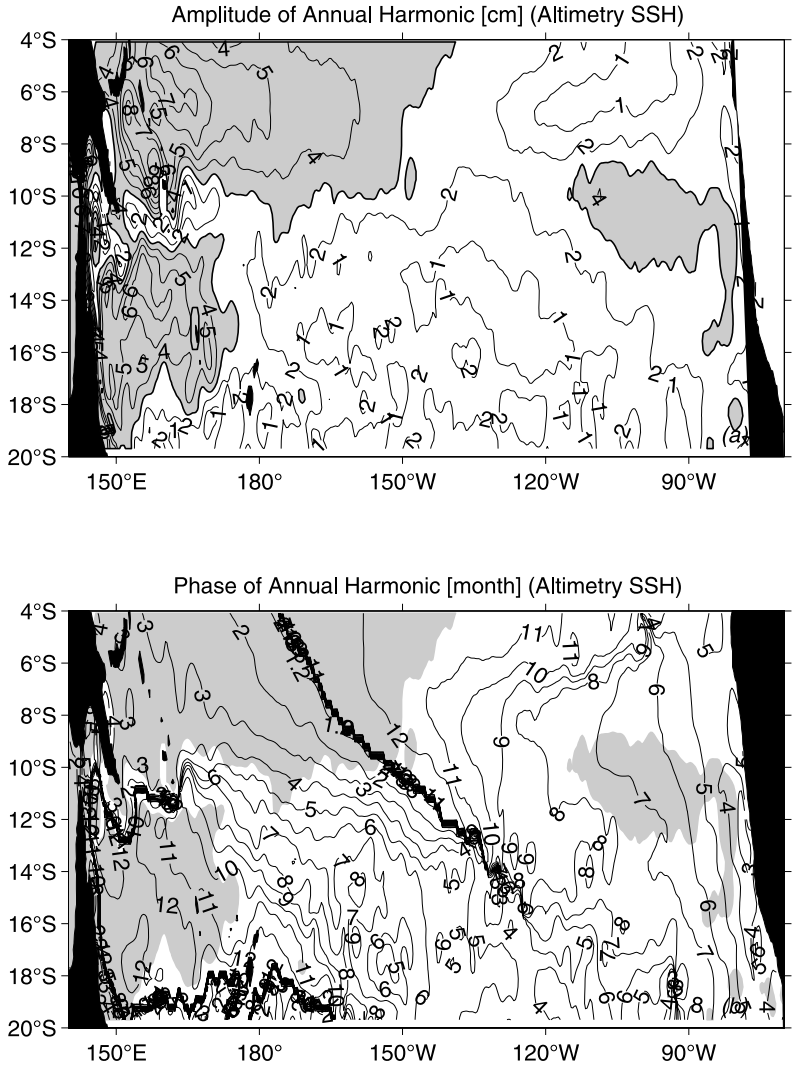

Figure 3. (a) Amplitude of the annual harmonic of the altimetric SSH anomaly in centimeters. (b) Phase of the annual harmonic in months. The phase is when the annual harmonic reaches the maximum, and it is in units of months ($1 \leq$ month < 13). The shading is where the corresponding harmonic amplitude exceeds 3 cm (see Figure 3a).

[14] Without the Rossby waves from the eastern boundary, the general solution of equation (1) is

$$h(x,y;t) = -\frac{1}{c_R}\int_{x_e}^{x} F\left(x', y; t + \frac{x-x'}{c_R}\right)dx', \tag{3}$$

which stands for forced Rossby waves. Two kind of forced Rossby waves, called resonantly forced Rossby waves and locally forced Rossby waves, are pertinent to the present study.

[15] The resonantly forced Rossby waves are forced by the wind, which moves westward at the same speed as the free Rossby waves in equation (1). Denoting the forcing such that $F(x, y, t) = A(y)e^{ik(x+c_R t)}$, the resonantly forced Rossby waves are then

$$h(x,t) = -\frac{A}{c_R}e^{ik(x+c_R t)}(x - x_e), \tag{4}$$

which has the same phase as the forcing F (i.e., angle of $e^{ik(x+c_R t)}$), but h's amplitude increases linearly westward.

[16] The locally forced Rossby waves are generated by the wind forcing not horizontally uniform but limited to the western part of the basin. We can idealize the forcing using either an exponential function maximized at the western boundary (denoted as x_W) or a Heaviside step function adjacent to the western boundary. In certain parameter ranges, both the idealized cases can result in the forced Rossby waves intensified westward but with different phase patterns.

2.1. $F(x, t) = Be^{-\frac{x-x_W}{L}}e^{i\omega t}$

[17] Here L measures how fast the wind forcing decreases exponentially away from the western boundary. After it is assumed that $e^{-\frac{x_e - x_W}{L}} \approx 0$, i.e., the wind does not extend to the eastern boundary, equation (3) becomes

$$h(x,t) = \frac{B}{\frac{c_R}{L} + i\omega}e^{-\frac{x-x_W}{L}}e^{i\omega t} = \frac{F(x,t)}{\frac{c_R}{L} + i\omega}.$$

Therefore h is also localized in the same form $e^{-\frac{x-x_W}{L}}$ as the forcing. There is a constant phase lag in h as compared to F.

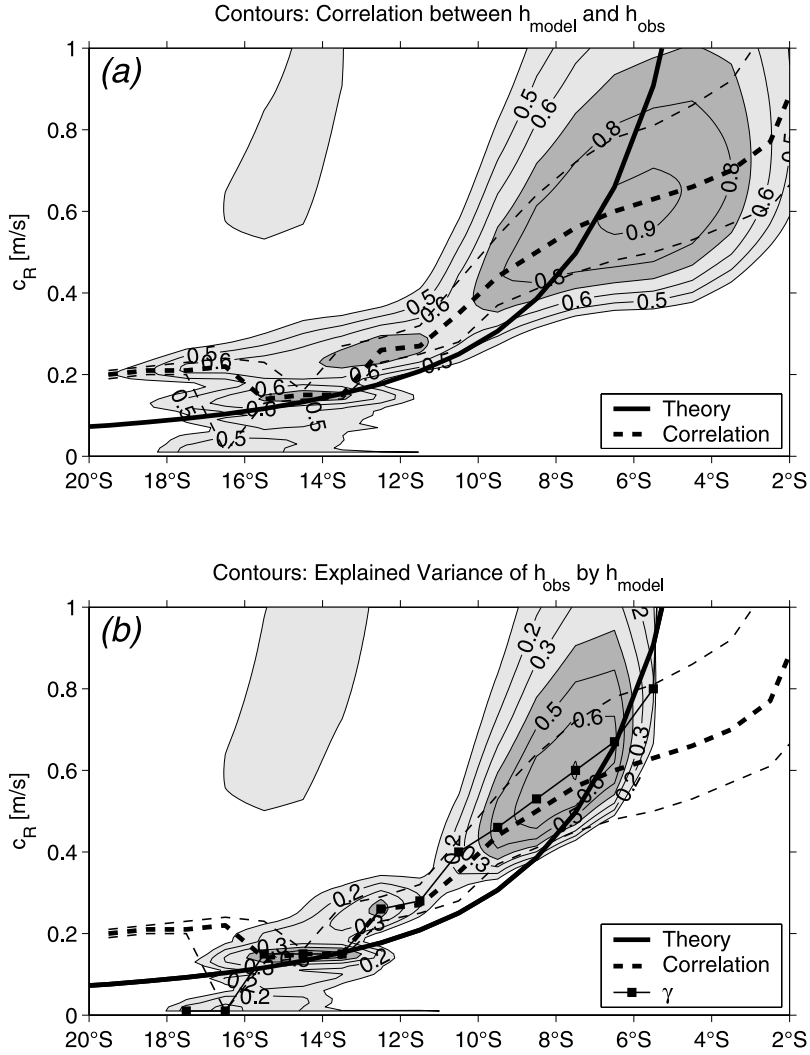

Figure 4. (a) Correlation between the model and altimetric SSH anomalies (contours) as function of c_R and latitude. The correlation coefficients are calculated at each 1° grid and averaged over 160°E–190°E. The thick dashed line shows the c_R where the maximum correlation reaches at each latitude. The thin dashed lines indicate the c_R range within 90% of the maximum correlation. The thick solid line is the theoretical c_R from *Chelton et al.* [1998]. (b) The explained variance of the altimetric SSH anomaly by the model SSH (contours) as function of c_R and latitude. The thick and thin dashed lines, as well as the thick solid line, are the same as in Figure 4a. The line with squares shows the c_R where the maximum explained variance reaches at each latitude.

The phase lag is $\tan^{-1}(\omega L/c_R)$. When ω is at the annual frequency, $c_R = 0.15\ \mathrm{m\,s^{-1}}$ and $L = 40°$ longitude, the phase lag is about 2.7 months (80°). As a reference, the phase lag will be exactly 3 months for the annual forcing (90°) if we omit the β term in equation (1). That is, if the wind forcing is proportional to $\cos(\omega t)$, the model h will be proportional to $\sin(\omega t)$.

2.2. $F(x, t) = B\mathcal{H}(x_L - x)e^{i\omega t}$

[18] Here $\mathcal{H}$ is the Heaviside step function. With $x_W < x_L < x_e$, the wind forcing is limited to the western basin. Equation (3) in this case becomes

$$h(x,t) = \frac{B}{\omega}\left[\sin\omega t - \sin\omega\left(t + \frac{x - x_L}{c_R}\right)\right] \tag{5}$$

$$= \frac{2B}{\omega}\cos\left[\omega t + \frac{\omega(x - x_L)}{2c_R}\right]\sin\frac{\omega(x_L - x)}{2c_R}. \tag{6}$$

Notice that we have assumed $h(x_L, t) = 0$. From equation (5), we see that the solution has two parts: the forced Rossby waves (the first term) and the free Rossby waves (the second term). In equation (6), if

$$0 \le \frac{\omega(x_L - x)}{2c_R} \le \frac{\omega(x_L - x_W)}{2c_R} \le \pi,$$

then $\sin\frac{\omega(x_L - x)}{2c_R}$ does not change sign, and it can be viewed as a spatial modulation of the oscillation $\cos\left[\omega t + \frac{\omega(x - x_L)}{2c_R}\right]$, which propagates westward at the doubled speed, $2c_R$ [*White*, 1977]. Furthermore, when

$$0 \le \frac{\omega(x_L - x)}{2c_R} \le \frac{\pi}{2}, \tag{7}$$

the spatial amplitude modulation increases westward from $x = x_L$. At the annual frequency, when $x_L - x$ is about

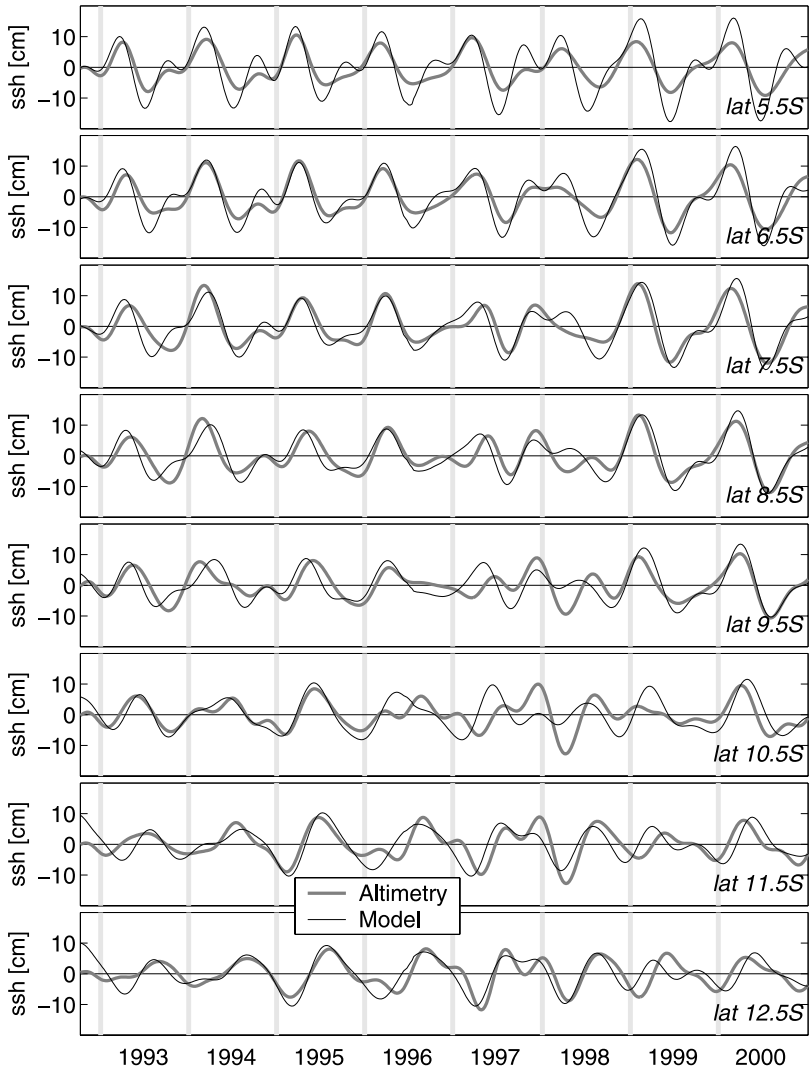

Figure 5. Time series of the sea surface height from the altimeter (thick lines) and from the model (thin lines) along 170°E. The six latitudes are shown in the lower right corner of each panel. The altimetric SSH anomaly is band passed between 150 days and 500 days, and the model SSH is the result forced by the ERS winds band passed between 150 days and 500 days.

22° longitude (half of the wavelength of the annual Rossby wave with $c_R = 0.15$ m s^{-1}), $\omega\frac{x_L - x}{2c_R} \approx \frac{\pi}{2}$. Physically, because the forced and free Rossby waves are only a half wavelength away from their origin, $x = x_L$, they tend to reinforce each other. Near x_L, the amplitude of h is small, and its phase is close to that of the forcing. The farther westward away from x_L, the more phase delay ($\frac{\omega(x - x_L)}{2c_R} < 0$ since $x < x_L$). When $x_L - x$ is about 22° longitude, the phase delay at x will be about 3 months (90°). Recall that the phase delay is also 3 months if there is no β effect. However, the phase lag in the no-β case is constant over the forcing region, but the phase lag here increases westward from zero at $x = x_L$.

3. Forced Rossby Waves

[19] We will in this section use the simple model of equation (1) to simulate the SECC seasonal variability seen in the altimetric SSH.

[20] The wind forcing is from the ERS weekly wind product from 1991 to 2001 with a horizontal resolution of 1° × 1°. To study the seasonal variability of the SECC, the forcing wind field was band passed first. The delimiting periods of the band are 150 days and 500 days. A detailed analysis on the wind forcing is given in the next section. The model result (h_{model}) is compared to the altimetric SSH anomaly (h_{obs}), which is band passed by the same filter and averaged over the 1° × 1° box centered at the wind forcing grid. In equation (1), we choose $g' = 0.04$ m s^{-2} so that the corresponding interval gravity wave speed is about 2.8 m s^{-1} if the upper layer mean depth of the 1.5-layer model is 200 m. As seen in equation (1), h is proportional to g', but no attempts are made in this study to adjust g' for a better comparison between the model result and the altimetric observation. We integrate equation (1) from the eastern boundary within 20°S and 2°S, but the model performs better in the SECC region approximately from 15°S to 5°S.

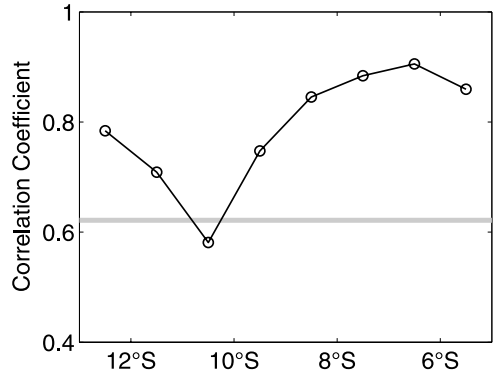

Figure 6. Correlation coefficients between the time series of h_{model} and h_{obs} along 170°E in Figure 5. The shaded line indicates the 95% significant correlation coefficient based on the Student-T test with 8 degrees of freedom, which corresponds to the 8 years time series.

[21] As in the work of *Meyers* [1979] and *Kessler* [1990], $c_R(y)$ in the model is treated as an unknown. For different $c_R(y)$, the correlations between h_{model} and h_{obs} are shown in Figure 4a. The maximum correlation at each latitude and the range within 90% of the maximum are highlighted. In the work of *Meyers* [1979] and *Kessler* [1990], no reasonable maxima could be found near the NECC. This does not happen near the SECC, probably because of the high-quality wind and SSH data sets used in this study. However, the maxima correlation does decrease near the SECC latitude. Toward the equator from the SECC, the maximum correlation increases, and so does its 90% range. For any c_R close to the theoretical c_R, h_{model} and h_{obs} are highly correlated. Notice that the correlation coefficient is more about the phase relationship between h_{model} and h_{obs}, in the sense that altering either h_{model} or h_{obs} by a constant factor will not affect the coefficient.

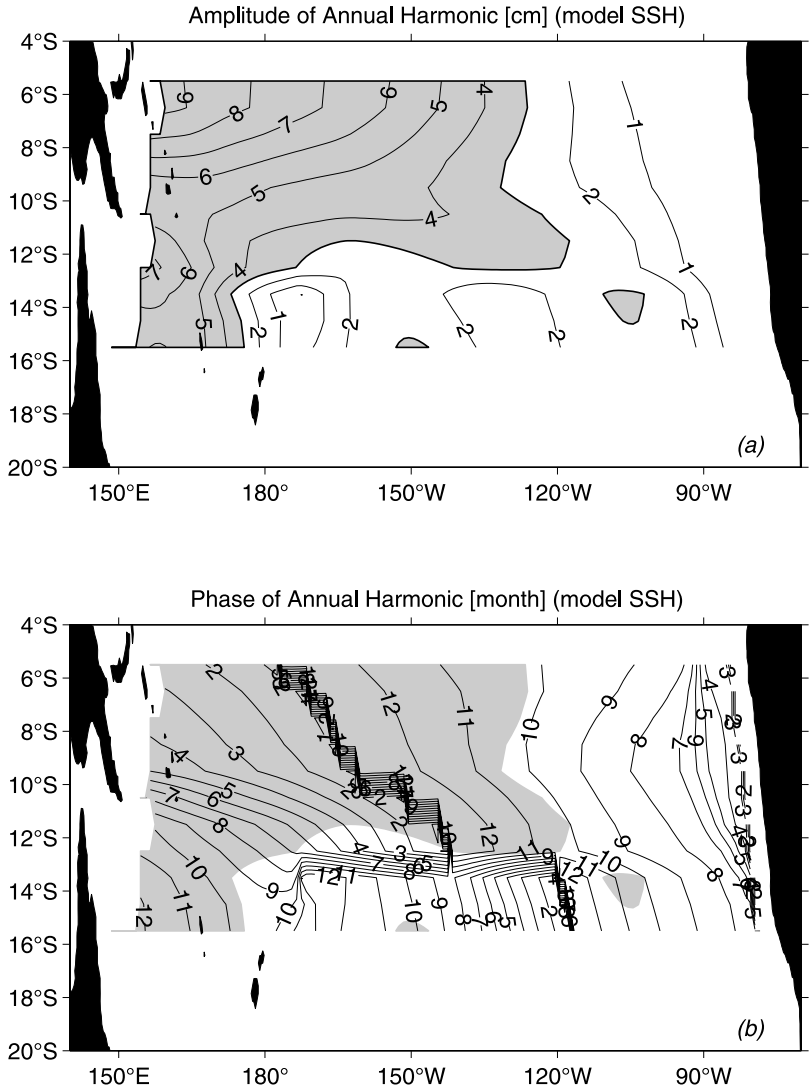

Figure 7. (a) Amplitude of the annual harmonics of the model result in centimeters. (b) Phase of the annual harmonics in months. The shading is where the corresponding harmonic amplitude exceeds 3 cm (see Figure 7a).

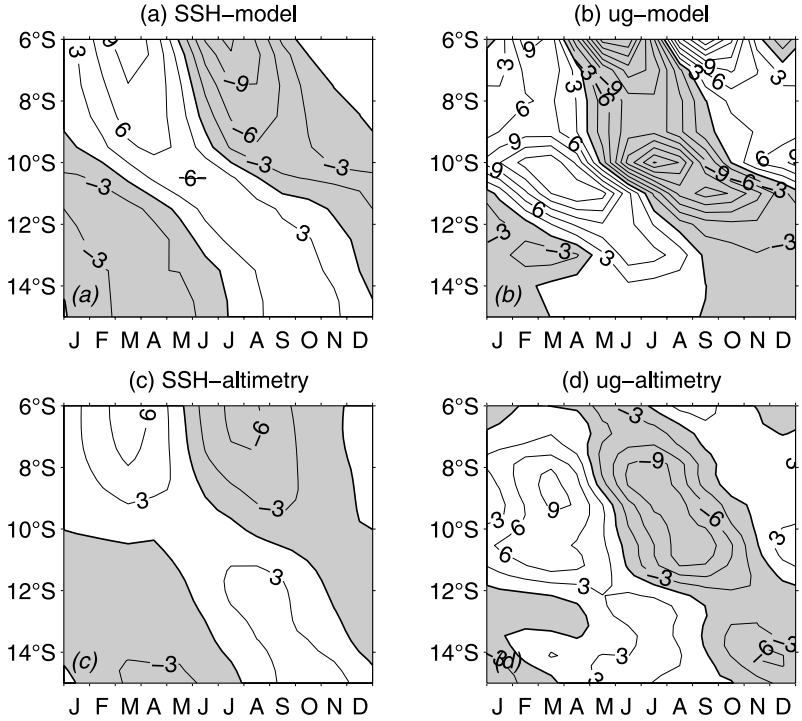

Figure 8. (a, b) The h_{model} monthly mean and the corresponding zonal geostrophic current along 170°E. (c, d) The h_{obs} monthly mean and the corresponding zonal geostrophic current along 170°E. Negatives are shaded. The contour units are centimeters (left column) and cm s^{-1} (right column). The h_{model} and h_{obs} monthly means are formed for more than 8 years of data, some of which are shown in Figure 5.

[22] Because of the large range of the correlation coefficient north of 10°S, another index, termed as explained variance, is defined as

$$\gamma = 1 - \frac{\sum_t (h_{\text{model}} - h_{\text{obs}})^2}{\sum_t h_{\text{obs}}^2},$$

and shown in Figure 4b. When the maximum correlation matches the maximum explained variance, we should have more confidence in the model. The match, occurring from 15.5°S to 5.5°S, indicates that the dynamics of the seasonal variability of the SECC is predominantly the forced long Rossby waves (i.e., equation (1)). The c_R value, used to generate the model result shown in the following, is chosen for the maximum γ at each latitude. From Figure 4b, c_R = 0.59, 0.23, and 0.13 m s^{-1} are observed near 7.5°S, 12.5°S, and 15°S, respectively.

[23] Figure 5 compares the model result, using c_R for maximum γ (the squares in Figure 4b), with the altimetric SSH along 170°E. The favorable agreement is illustrated in Figure 6 by the significant correlation coefficients between altimetry h_{obs} and h_{model}, except at 10.5°S where the wind forcing reaches a local minimum and the two types of forced Rossby waves merge as will be shown in the next section. Also notice that the amplitude, but not the phase, at latitude 5.5°S is less satisfactory. This corresponds to the fact that the explained variance is low at 5.5°S (Figure 4b). As mentioned earlier, g' can directly affect the amplitude of h_{model}; a constant g' for the whole region in this study may be too simple.

[24] To show the model result on the basin scale, the annual harmonic analysis is performed on the model SSH in the same way as on the altimetric SSH (Figure 3). As seen in the time series along 170°E in Figure 5, the annual harmonics are the dominant signals. Comparing the amplitudes of the h_{model} annual harmonics (Figure 7a) with those of h_{obs} (Figure 3a) reveals that the model reproduces the basic features of the altimetric observation west of 120°W. Both have a local minimum near 10°S. The large amplitude (>3 cm) areas correspond quite well to each other. The signal near the eastern boundary (within about 10° longitude from the coast) in h_{obs} is entirely missed in h_{model}; it could be Rossby waves initiated by coastal Kelvin waves from the equator [*Vega et al.*, 2003], which are excluded in the model by our eastern boundary condition ($h_{x=x_e}$ = 0). Near the northern edge of the domain, the amplitude in h_{model} is about 30% larger, and this difference could again be attributable to the constant g' used in our model.

[25] In Figures 7b and 3b, we compare the phases of the annual harmonics from h_{model} and the altimetric SSH anomalies. At about 10°S in the western basin, there is a phase jump in h_{model}, although it appears less sharp as in the altimetric SSH data, possibly due to the 1° resolution of the h_{model}. For the areas with large amplitudes (>3 cm), the phases in h_{model} are generally within 1 month of those in the altimetric SSH anomalies.

[26] The phase jump in the seasonal SSH field is critical for the seasonal changes of the SECC. Figure 8 shows the monthly h_{model} and h_{obs} fields, as well as the corresponding surface zonal geostrophic flows along 170°E. The strong zonal geostrophic flows in the right column of Figure 8

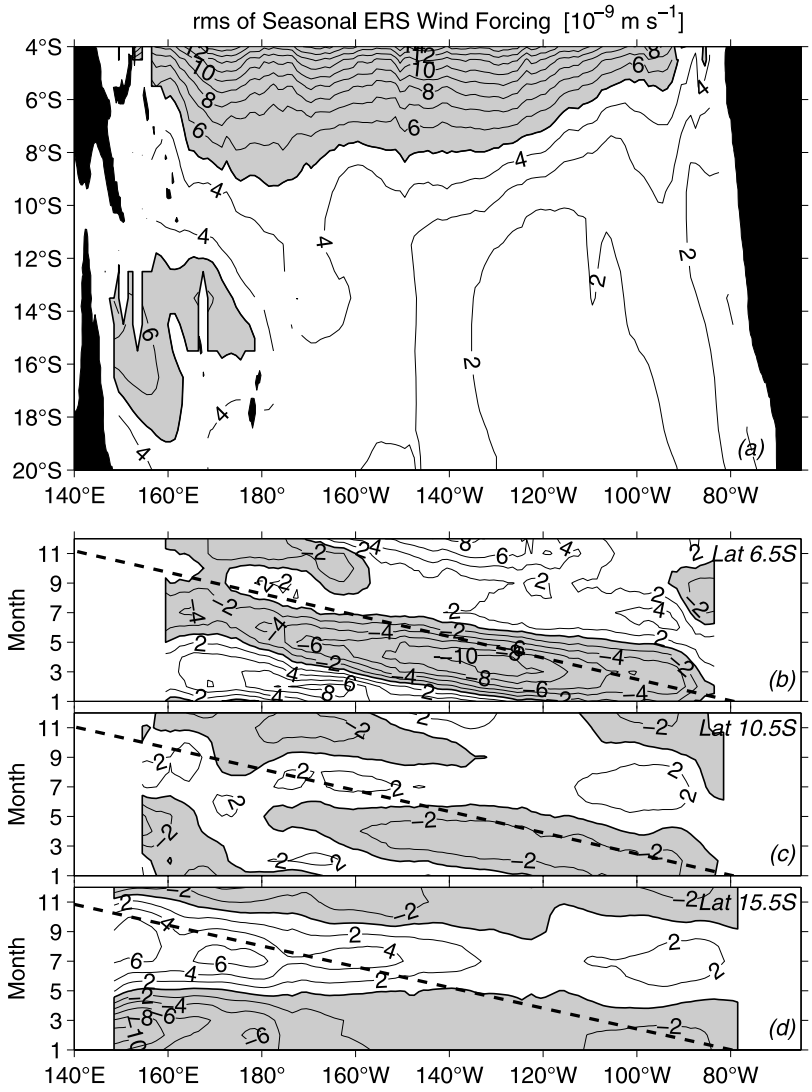

Figure 9. (a) RMS amplitude of the band-passed ERS wind forcing (August 1991 to January 2001). (b, c, d) Hovmoller diagrams of the wind forcing at latitudes 15.5°S, 10.5°S, and 6.5°S. The seasonal cycles are the average of the more than 9 years data. In Figures 9b, 9c, and 9d, negatives are shaded, and the dashed lines indicate the westward propagation speed 0.59 m s^{-1}, which is the optimized c_R at 7.5°S in Figure 4b and also corresponds to the vertical dashed line in Figure 10. All are in unit 10^{-9} m s^{-1}.

correspond to the latitudinal phase jump of SSH anomalies in the left column of Figure 8. In other words, the latitudinal phase jump determines the location of the seasonal SECC. The strong geostrophic flow observed by the altimeter (Figure 8d) is 1°–2° more spread to the north than in the model (Figure 8b), but its seasonal variability (maximum eastward flow around March and maximum westward flow around September) is the same.

4. Wind Forcing

[27] As detailed in section 3, the Rossby wave model reproduced the seasonal variability of the SECC well. Except for c_R, which is chosen independently at each latitude for the maximum explained variance (γ, Figure 4b), the dynamics of the model are rather simple. Clearly, the wind forcing plays an important role in the behavior of the Rossby waves.

[28] Figure 9a shows the RMS amplitude of the ERS band-passed wind forcing. There is a local minimum near 10°S in the western basin, where a local minimum in the altimetric SSH in Figure 3a is also found. The local minimum suggests that the winds north and south of 10°S may have different characteristics, which are demonstrated in the Hovmoller diagrams in Figures 9b, 9c, and 9d.

[29] At 6.5°S (Figure 9b), the wind forcing is clearly propagating westward, approximately at the speed 0.59 m s^{-1}. We also see that the wind forcing is stronger in the first half of the year. This wind system is part of the annual tropical Pacific wind influenced by the large-scale atmosphere-ocean interaction centered in the cold tongue in the eastern Pacific. As showed by *Wang* [1994], the annual perturbation (departure of climatological monthly mean from the long-term mean) of sea surface temperature displays simultaneous intensification and spatial expansion during its development from January to May, and the

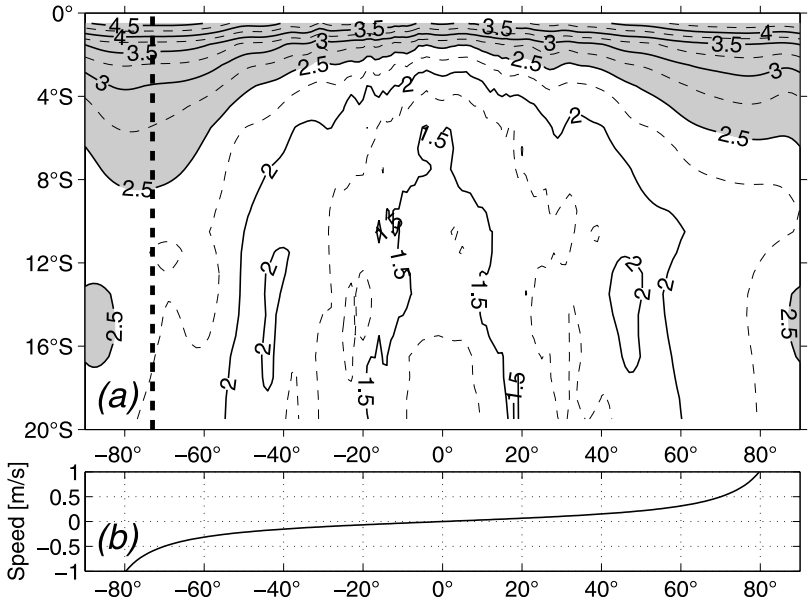

Figure 10. (a) "Energy" in log scale from the Radon transform analysis of the band-passed ERS wind forcing (see text for a brief introduction of the method). The thick dashed lines indicate the propagation speed 0.59 m s^{-1}, which is the γ optimized c_R at 7.5°S in Figure 4b. (b) The conversion from θ to the propagation speed c_R.

westward phase propagation, inferred from the 0.6°C SST anomaly westward expansion, is about 0.68 m s^{-1}. The propagation speed is close to that of surface wind (Figure 9b), indicating that SST and surface wind are coupled. At 15.5°S (Figure 9d), the wind forcing is dominantly stationary and occurs mainly in the western basin. The wind system is due to the eastward intrusion of the Western Pacific Monsoon [*Wang et al.*, 2000]. The wind forcing at 10.5°S (Figure 9c) is the mixture of the two wind systems.

[30] To be more quantitative about the propagation in the wind forcing, the Radon analysis [*Hill et al.*, 2000] is applied to the band-passed ERS wind-forcing data. Imagine that the wind-forcing F at each latitude is a two-dimensional array with time t to the vertical and longitude x to the right. In the rotated coordinate (t', x'), which is θ° clockwise from the vertical, the Radon analysis calculates the following "energy" as function of θ, as well as latitudes (Figure 10a):

$$E = \int \left\{ \int F(x', t')dt' \right\}^2 dx'.$$

If F has a significant propagation signal, $\int F(x', t')dt'$ tends to sum up (cancel each other) so that E is large (small) when t' is parallel (perpendicular) to the propagation direction. The slope of t'-axis in (x, t) coordinate is $\tan(90 - \theta)$ or $\frac{\Delta x}{c_R \Delta t}$ from $x = c_R t$, where Δx and Δt are the sampling intervals of F in x and t, so that one can convert θ to the propagation speed c_R (Figure 10b). The enhanced westward propagation energy in the wind forcing north of 10°S is clear. The Radon analysis also shows that the energy peak is broad within 0.3–1.5 m s^{-1} in terms of propagation speed. South of 10°S, the stationary (propagating at an infinity speed) energy is dominant.

[31] We have also applied the annual harmonic analysis to the ERS wind forcing (Figures 11a and 11b). North of 10°S, the westward decrease of the annual harmonic amplitudes of the wind forcing contrasts to the westward increase of those of the altimetric SSH in Figure 3a. The amplitude distribution is similar to that of the standard deviation (Figure 9a). However, the amplitude of the annual harmonics in the western basin north of 10°S is noticeably decreased, because, as shown in the Hovmoller diagram in Figure 9b, the semiannual component is larger in the western basin (two positive extrema and two negative extrema) than in the eastern basin. The phases of the forcing wind (Figure 11b) are consistent with Figures 9b, 9c, and 9d. That is, north of 10°S, the wind forcing propagates westward, and south of 10°S, especially in the western basin, the forcing is stationary. Comparing Figure 11b with Figure 3b, north of 10°S the phase of the wind forcing matches that of the altimetric SSH anomaly within 1 month; south of 10°S, the phase of the wind forcing matches that of the altimetric SSH anomaly only near the center of the basin; toward the west, the phase of the altimetric SSH anomalies increases while that of the wind forcing remains nearly constant.

[32] The intercomparison among the phases and amplitudes of the altimetric SSH anomaly (Figure 3), h_{model} (Figure 7) and wind forcing (Figure 11) suggests that the Rossby waves are resonantly forced north of 10°S and are locally forced south of 10°S. The resonantly forced Rossby waves have the same phase as the wind forcing, but their amplitude increases westward while the amplitudes of the wind forcing do not. The locally forced Rossby waves have the same phase as the wind forcing at its eastern edge (approximately near the center of the basin, see contours "8" in Figures 7b and 11b), and have their phases increase westward. While the westward phase increase is less than 90° (3 months for the annual Rossby waves), the amplitude of the locally forced Rossby waves increases westward. The westward phase increase of the locally forced Rossby waves indicates that the Heaviside step function may be a better representation of the wind field south of 10°S than the exponential function (compare section 2), although the

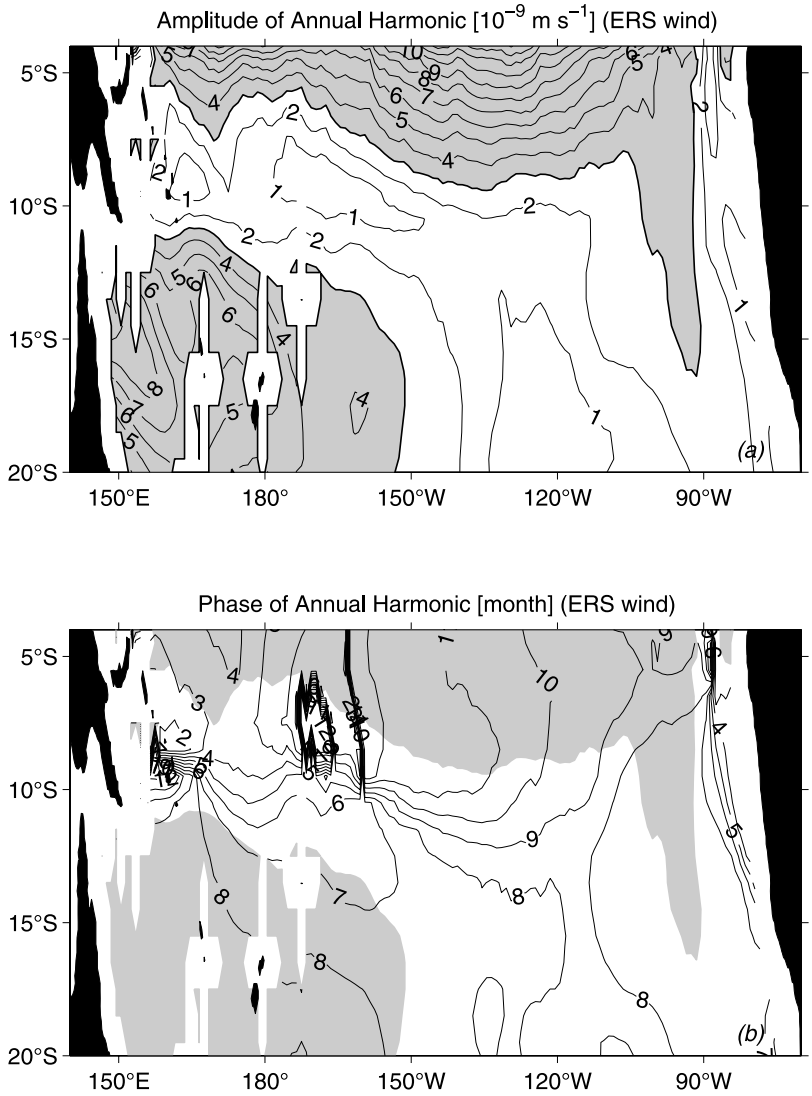

Figure 11. (a) Amplitude of the annual harmonics of the wind forcing F in 10^{-9}m s^{-1}. (b) Phase of the annual harmonics in months. The shading is where the corresponding harmonic amplitude exceeds 3×10^{-9}m s^{-1} (see Figure 11a).

observed wind forcing field in Figure 7a indicates a more complex structure than the Heaviside step function.

[33] As shown in Figure 12, the resonantly forced Rossby waves north of 10°S propagate westward close to the observed speed c_R (compare the solid squares and the line with pluses in Figure 12). South of 12°S, on the other hand, the locally forced Rossby waves are found to propagate westward at the doubled speed $2c_R$.

5. Summary and Discussion

[34] Using a 1.5-layer long Rossby wave model, we demonstrated the relationship between the seasonal variability of the SECC and the two types of forced Rossby waves: resonantly forced Rossby waves north of 10°S and locally forced Rossby waves south of 10°S. Both types of waves are westward intensified in the western basin of the tropical South Pacific Ocean but have different phases. The latitudinal phase jump of the SSH annual harmonics leads to the seasonal variability of the SECC. The resultant zonal geostrophic current of the SECC has a maximum in March and a minimum in August.

[35] There are two annual wind forcing systems in the SECC region. North of 10°S, the wind forcing is part of the annual tropical Pacific wind due to the large-scale atmosphere-ocean interaction centered in the cold tongue in the eastern Pacific [*Wang*, 1994]. South of 10°S in the western basin, the wind forcing is the eastward intrusion of the Western Pacific Monsoon [*Wang et al.*, 2000].

[36] Evidence for the atmosphere-ocean coupled Rossby waves was presented by *White* [2001]. Both the coupled Rossby waves and the resonantly forced Rossby waves have the same westward propagation speed as the wind forcing. The resonantly forced Rossby waves intensify westward while the wind forcing does not. Meanwhile, the coupled Rossby waves should have a similar amplitude pattern to that of the wind. This discrepancy between the amplitudes of the wind and SSH patterns is the main factor that supports the resonantly forcing mechanism north of 10°S. The locally forced Rossby waves south of 10°S are different

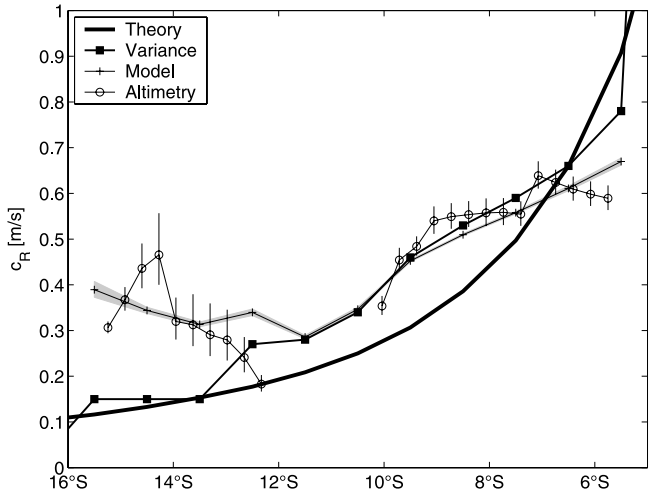

Figure 12. Rossby wave westward propagation speeds as functions of latitudes in the SECC region. Both the thick solid line (Theory) and the line with squares (Variance) are the same as those in Figure 4b. The line with crosses (Model) is the phase speeds inferred from the model annual harmonics by the linear regression of the phases with amplitude larger than 3 cm s^{-1} (shaded area in Figure 7b). The shaded area associated with the line with crosses is the 95% confidence interval of the linear regression. The line with circles (Altimetry) is inferred in the same way as for the line with crosses, but from the annual harmonics of the altimetric SSH anomaly.

from those from the Ekman pumping mechanism: a balance between the stretching term and the Ekman pumping without the β term in the potential vorticity equation; the doubled phase propagation for the locally forced Rossby waves, not for the Ekman pumping mechanism, was identified in the western basin south of 10°S.

[37] As shown by *Wang* [1994], the annual wind forcing north of 10°S is part of the large-scale coupled air-sea phenomenon, in which the perturbations of SST, sea level pressure, and wind fields together propagate westward. The difference between the coupled air-sea phenomenon discussed by *Wang* [1994] and the coupled Rossby waves studied by *White* [2001] is how the SST variation is generated. In the coupled Rossby waves in the South Pacific, the SST variation is due to the advection of the mean temperature by the geostrophic flow of the oceanic Rossby waves. The SST variation responsible for the wind north of 10°S is the annual cycle of the equatorial cold tongue, which has nothing to do with the oceanic Rossby waves. In other words, oceanic Rossby waves are forced and not part of the coupled air-sea phenomenon discussed by *Wang* [1994].

[38] The goal of this study is to understand the dynamics of the seasonal variability of the SECC. Therefore we did not attempt to adjust the 1.5-layer model parameters, such as g' and the eastern boundary condition. A better understanding of the seasonal modulation of the SECC is important, as it determines the regional, seasonal generation of mesoscale eddies [*Qiu and Chen*, 2004]. In addition to its seasonal variability, interannual changes in the SECC have also been observed along 165°E during 1984–1988 [*Delcroix*, 1998]. Future studies are needed to clarify how the interannual changes of the SECC are related to tropical El Niño–Southern Oscillation events and the regional and basin-scale wind forcing.

[39] **Acknowledgments.** Detailed comments by the editor James Richman and two anonymous reviewers helped to improve an earlier version of the manuscript significantly. The merged T/P and ERS-1/2 altimeter data are provided by the CLS Space Oceanography Division as part of the Environment and Climate EU ENACT project and with support from CNES. Support from NASA through contracts 1207881 and 1228847 is gratefully acknowledged.

References

Chelton, D. B., and M. G. Schlax (1996), Global observations of oceanic Rossby waves, *Science*, *272*, 234–238.

Chelton, D. B., R. A. deSzoeke, and M. G. Schlax (1998), Geographical variability of the first baroclinic Rossby radius of deformation, *J. Phys. Oceanogr.*, *28*, 433–460.

Conkright, M. E., R. A. Locarnini, H. E. Garcia, T. D. O'Brien, T. P. Boyer, C. Stephens, and J. I. Antonov (2002), *World Ocean Atlas 2001: Objective Analyses, Data Statistics, and Figures*, *Internal Rep. 17*, 17 pp., Natl. Oceanic and Atmos. Admin., Silver Spring, Md.

Delcroix, T. G. (1998), Observed surface oceanic and atmospheric variability in the tropical Pacific at seasonal and ENSO timescales: A tentative overview, *J. Geophys. Res.*, *103*(C9), 18,611–18,633.

Delcroix, T., G. Eldin, M. H. Radenac, J. M. Toole, and E. Firing (1992), Variation of the western equatorial Pacific Ocean, 1986–1988, *J. Geophys. Res.*, *97*(C4), 5423–5445.

Fu, L.-L., and D. B. Chelton (2001), Large-scale ocean circulation, in *Satellite Altimetry and Earth Science: A Handbook of Techniques and Applications*, edited by L.-L. Fu and A. Cazenave, 463 pp., Academic, San Diego, Calif.

Fu, L.-L., and B. Qiu (2002), Low-frequency variability of the North Pacific Ocean: The roles of boundary- and wind-driven baroclinic Rossby waves, *J. Geophys. Res.*, *107*(C12), 3220, doi:10.1029/2001JC001131.

Gouriou, Y., and J. Toole (1993), Mean circulation of the upper layers of the western equatorial Pacific Ocean, *J. Geophys. Res.*, *98*(C12), 22,495–22,520.

Hill, K., I. Robinson, and P. Cipollini (2000), Propagation characteristics of extratropical planetary waves observed in the ATSR global sea surface temperature record, *J. Geophys. Res.*, *105*(C9), 21,927–21,945.

Kessler, W. (1990), Observation of long Rossby waves in the northern tropical Pacific, *J. Geophys. Res.*, *95*(C4), 5183–5217.

Kessler, W., G. Johnson, and D. Moore (2003), Sverdrup and nonlinear dynamics of the Pacific equatorial currents, *J. Phys. Oceanogr.*, *33*, 994–1008.

Meyers, G. (1979), On the annual Rossby wave in the tropical North Pacific Ocean, *J. Phys. Oceanogr.*, *9*, 663–674.

Qiu, B., and S. Chen (2004), Seasonal modulations in the eddy field of the South Pacific Ocean, *J. Phys. Oceanogr.*, in press.

Qiu, B., W. Miao, and P. Muller (1997), Propagation and decay of forced and free baroclinic Rossby waves in off-equatorial oceans, *J. Phys. Oceanogr.*, *27*, 2405–2417.

Qu, T., and E. J. Lindstrom (2002), A climatological interpretation of the circulation in the western South Pacific, *J. Phys. Oceanogr.*, *32*, 2492–2508.

Reverdin, G., C. Frankignoul, E. Kestenare, and M. McPhaden (1994), Seasonal variability in the surface currents of the equatorial Pacific, *J. Geophys. Res.*, *99*(C10), 20,323–20,344.

Tomczak, M., and J. S. Godfrey (1994), *Regional Oceanography: An Introduction*, 422 pp., Pergamon, New York.

Vega, A., Y. duPehoat, B. Dewitte, and O. Pizarro (2003), Equatorial forcing of interannual Rossby waves in the eastern South Pacific, *Geophys. Res. Lett.*, *30*(5), 1197, doi:10.1029/2002GL015886.

Wang, B. (1994), On the annual cycle in the tropical eastern central Pacific, *J. Clim.*, *7*, 1926–1942.

Wang, B., R. Wu, and R. Lukas (2000), Annual adjustment of the thermocline in the tropical Pacific Ocean, *J. Clim.*, *13*, 596–1942.

White, W. (1977), Annual forcing of baroclinic long waves in the tropical North Pacific Ocean, *J. Phys. Oceanogr.*, *7*, 50–61.

White, W. (2001), Evidence for coupled Rossby waves in the annual cycle of the Indo-Pacific Ocean, *J. Phys. Oceanogr.*, *31*, 2944–2957.

WOCE Data Products Committee (2002), WOCE Global Data, Version 3.0, *Rep. 180/02*, Southampton, England.

S. Chen and B. Qiu, Department of Oceanography, University of Hawaii at Manoa, 1000 Pope Road, Honolulu, HI 96822, USA. (schen@soest.hawaii.edu; bo@soest.hawaii.edu)